Journal of Molecular Liquids 390 (2023) 123027

Contents lists available at ScienceDirect

Journal of Molecular Liquids

journal homepage: www.elsevier.com/locate/molliq

Preparation of a composite sensor based on a fluorescent and magnetic molecular imprint polymer for metronidazole extraction–detection

Laís Mendes Alvarenga [a], Cristiane dos Reis Feliciano [a], Bruno Giordano Alvarenga [b], Hauster Maximiler Campos de Paula [c], Yara Luiza Coelho [a,c], Luis Henrique Mendes da Silva [c], Luiz Fernando Gorup [a,e], Mariane Gonçalves Santos [d], Luciano Sindra Virtuoso [a,*]

[a] Colloid Chemistry Group, Chemistry Institute, Federal University of Alfenas (UNIFAL-MG), 700 Gabriel Monteiro da Silva street, 37130-000 Alfenas-MG, Brazil
[b] Laboratory of Surfactant Physical-Chemistry, Pontifical Catholic University of Rio de Janeiro, Rio de Janeiro 22451-900, RJ, Brazil
[c] Colloidal and Macromolecular Green Chemistry Group (QUIVECOM), Department of Chemistry, Federal University of Viçosa, Av. P. H. Rolfs s/n, 36570900 Viçosa, MG, Brazil
[d] Toxicants and Drugs Analysis Laboratory – LATF, Faculty of Pharmaceutical Sciences, Federal University of Alfenas – Unifal-MG, 700 Gabriel Monteiro da Silva street, 37130-000 Alfenas, MG, Brazil
[e] Interdisciplinary Laboratory of Electrochemistry and Ceramics- LIEC, Department of Chemistry, UFSCar- Federal University of São Carlos, Rod. Washington Luis km 235, CP 676, São Carlos SP, Brazil, CEP 13565-9905

ARTICLE INFO

Keywords:
Molecularly imprinted polymer
Metronidazole selective sensor
Magnetic nanoparticles
Real-time analysis
Surface Plasmon Resonance

ABSTRACT

We developed a metronidazole (MNZ)-selective sensor, combining magnetic and fluorescent molecularly imprinted polymers (MFMIP) with a non-imprinted reference composite (MFNIP). Using isothermal titration calorimetry (ITC), we optimized the MNZ-to-APTES ratio during polymerization, obtaining a specific MNZ-APTES bonded complex ($K_b = 2.575 \times 10^3$ L/mol, $\Delta H^\circ = -1.079$ kJ mol^{-1}, $T\Delta S^\circ = 18.389$ kJ mol^{-1}, and $\Delta G^\circ = -19.468$ kJ mol^{-1}). The MFMIP composite, incorporating Fe_3O_4@TEOS magnetite nanoparticles and CdTe@TGA quantum dots, exhibited cavity-specific interactions with MNZ, as confirmed by surface plasmon resonance (SPR) studies. Compared to MFNIP, the MFMIP sensor demonstrated superior selectivity in water samples (5–60 μM, with LOD and LOQ values of 1.28 and 5.00 μM), and even in the presence of interferents. In addition, the use of CdTe quantum dots enabled real-time analysis via Stern–Volmer quenching mechanisms without complex sample preparation. In conclusion, our MFMIP sensor offers sensitive and selective MNZ detection. It presents practical advantages, including real-time analysis and ease of handling, making it a promising extraction–determination system for trace concentrations of MNZ.

1. Introduction

Since their discovery and development, antibiotics have played a vital role in the treatment of veterinary, human, plant, and even bee diseases. Therefore, the presence of antibiotic residues in food and aqueous matrices may be a consequence of disease treatment [1]. The accumulation of antibiotic residues in the body can result in the development of resistant bacteria and toxic and carcinogenic reactions [2].

Metronidazole (MNZ; Figure S1, Supplementary Material) is the most commonly used nitroimidazole antibiotic, which is well known for its antimicrobial properties and action against anaerobic bacteria. However, several studies have noted that MNZ causes genotoxic, carcinogenic, and mutagenic side reactions [3,4]. The accumulation of MNZ in the human body can cause seizures, peripheral neuropathy, ataxia, and the development of bacterial resistance to it [1,5]. Therefore, the concentration of this drug in human blood plasma, water, and foods such as meat, milk, and honey must be controlled [2,6,7].

Various methods such as mass spectrometry [8], high-performance liquid chromatography (HPLC) [9], microfluidic cartridge setup [10], and high-performance thin film chromatography [11] have been used for the detection of antibiotics in various matrices (water, honey, milk, and tissues of edible animals). Although efficient, these analyses are expensive, difficult to handle, and/or require sample pretreatment, which increases analysis time [12,13]. Composite sensors based on molecularly imprinted polymers (MIPs) may be used to overcome these limitations. These sensors contain fluorescent probes that generate

* Corresponding author.
E-mail address: luciano.virtuoso@unifal-mg.edu.br (L. Sindra Virtuoso).

https://doi.org/10.1016/j.molliq.2023.123027
Received 7 April 2023; Received in revised form 25 August 2023; Accepted 7 September 2023
Available online 9 September 2023

signals via fluorescence spectroscopy [14–16]. The detection of analytes using fluorescence spectroscopy has become very attractive, owing to its high recognition capacity, sensitivity, selectivity, simplicity, and responsivity, low cost, and capacity for real-time detection [15–17].

MIPs exhibit excellent chemical, thermal, and mechanical stabilities, as well as selective recognition and application in diverse matrices. In typical sol–gel in-situ syntheses of MIPs, monomer complexes enable the formation of imprinted polymers containing functional groups that complement certain parts of the molecules used as the templates. These complexes undergo polymerization, which is promoted by crosslinking agents and favors the formation of porous polymeric matrices. Subsequently, the templates are eliminated by cleaving the previously occurring interactions. Thus, the final materials retain only molecular "memories" of the templates, constituted by cavities complementary to them in size, shape, and position of certain functional groups [16,18,19].

Thus, MIPs exhibit selective sites that enable specific interactions with analytes, significantly reducing the possibility of interference during analysis. This assigns to MIPs high selectivity and significant potential as artificial recognition materials [18,19]. To compare selectivities and sensitivities, non-unprinted polymers (NIPs), which lack the template molecules and selective cavities, are synthesized [3,16].

Various materials can be added during MIP synthesis to obtain a final product with specific characteristics. To attribute fluorescent properties to MIPs, quantum dots (QDs) may be used. Because they are luminescent nanomaterials, QDs exhibit excellent quantum yields and recognition capabilities while interacting with molecules and are widely used for sensing, bio-imaging, and diagnosis [15,16].

QDs can also be used as recognition and transduction elements for MIPs. The presence of a fluorescent signal, owing to the incorporation of QDs in the polymeric matrix, increases the utility of MIP-based sensors, as the addition of QDs can improve the precision and efficiency of the analysis. In addition, QDs promote an increase in sensor selectivity and enable the recognition and direct quantification of target analytes [3,14]. Cadmium telluride (CdTe) QDs are semiconductor nanocrystals with diverse applications, owing to their high stability in aqueous media [20,21].

Owing to their magnetism, MNPs can be easily isolated and separated from complex multiphase media by the application of a magnetic field. The separated material can be re-suspended by pausing the application of the magnetic field [22]. The use of Fe_3O_4 and MIPs can facilitate a simple and fast recovery of polymers, eliminating the need for additional procedures such as centrifugation and filtration [23].

Various morphological, chemical, thermal, and functional techniques for the characterization of MIP/NIP particles have been used in the broad evaluation of composites fabricated using them [24–28]. In particular, the selective binding of the target molecule to the MIP-printed cavity has been investigated to better understand the molecular events related to the kinetics and thermodynamics of these interactions. MIP structures on surfaces such as immobilized films are often investigated using surface plasmonic resonance (SPR) [29–33]. Recently, MIP and SPR technology has been applied in several domains, for example, the selective and unlabeled detection of HSA protein in biological samples [34] detection of amoxicillin residues in egg extracts [35] and sulfamethoxazole detection [36]. SPR is widely known to enable fast, real-time, and highly sensitive analyses of a wide range of target substances, with a good reliability and signal stability [37–39].

Herein, we synthesized and characterized magnetic and fluorescent imprinted composites (MFMIPs) for MNZ determination. Molecular imprinting was performed on the surface of the nanoparticles using the Stober method of in-situ polymerization. In the MIPs, selective recognition cavities, in which MNZ could rebind and selectively interact with fluorescent nanocrystals, resulted in quenching. Fe_3O_4@TEOS NPs attributed superparamagnetic characteristics to the biosensor, facilitating its extraction from aqueous matrices. The interactions of MFMIP and the non-printed reference MFNIP with the target molecule, MNZ, were studied using SPR, which facilitated the determination of the kinetic parameters of these interactions. MFMIP was used to detect trace concentrations of MNZ in water samples.

2. Experimental section

2.1. Materials

All chemicals and reagents used in this study were of analytical grade and did not require further purification. Thioglycolic acid (TGA), (3-aminopropyl) triethoxysilane (APTES), cadmium chloride hexahydrate ($CdCl_2{\cdot}6H_2O$), ammonium hydroxide (NH_4OH), methanol (CH_3OH), sodium tellurite ($NaTe_2O_3$), tetraethoxysilane (TEOS), sulfamethoxazole (SMX), 1-butyl-3-methylimidazoliumchloride ([Bmim]Cl), and metronidazole (MNZ) were supplied by Sigma-Aldrich (USA). Sodium hydroxide (NaOH) was obtained from Vetec Química fina (Brazil) and sodium borohydride ($NaBH_4$) from Nuclear (Brazil). Dibasic sodium phosphate (Na_2HPO_4) and sodium phosphate monohydrate ($NaH_2PO_4{\cdot}H_2O$) were purchased from Vetec (Brazil). CM5 sensor chips and coupling reagents (N-ethyl-N'-(dimethylaminopropyl) carbodiimide (EDC), N-hydroxysuccinimide (NHS), and ethanolamine hydrochloride were purchased from GE Healthcare (USA). Deionized water was obtained from a MILLI-Q water purification system (18.2 M Ω cm resistivity, Millipore, USA) and used as a solvent.

2.2. Rational planning and preparation of composites

2.2.1. Isothermal titration calorimetry (ITC) analysis

The enthalpy changes associated with the MNZ–APTES interactions at 298.15 ± 0.1 K were recorded using an isothermal titration microcalorimeter PEAQ-ITC (Malvern Instruments). Initially, MNZ (1 mM) and APTES (40 mM) solutions were prepared in water-methanol (1:1) and degassed before titration. Subsequently, the sample and reference cells were loaded with 195 μL of the MNZ solution, and the APTES solution was injected into them using a syringe. After baseline stability had been achieved, 19 aliquots of the monomer solution (2 μL each) were injected into the MNZ solution. A dilution experiment was performed by replacing the MNZ solution with the pure solvent (water/methanol 1:1). The samples were constantly stirred at 500 rpm to ensure uniform mixing. The initial interval and delay time between successive injections was 3600 and 180 s, respectively. Raw data was obtained as a plot of potency (μW) against time. These data were integrated to obtain a plot of the observed enthalpy change (ΔH_{obs}) per mole of the injected APTES. The ΔH_{obs} associated with the APTES dilution was subtracted from the corresponding ΔH_{obs} of the MNZ–APTES mixing to obtain the real apparent enthalpy change ($\Delta H_{app-int}$) of the MNZ–APTES interactions. The $\Delta H_{app-int}$ values for MNZ–APTES interactions were finally plotted as a function of the molar ratio of APTES/MNZ and fitted to a single set of identical sites (SSIS) model (Martinez et al., 2013; Eq. (1) to obtain the binding constant (K_b), binding stoichiometry number (n), and calorimetric standard enthalpy change (ΔH^o_{cal}) for MNZ–APTES complex formation.

$$Q = \frac{\Delta H^0 V_c}{2K_b}\left[1 + K_b[\mathrm{L}]_T + nK_b[\mathrm{R}]_T - \sqrt{\left(1 + K_b[\mathrm{L}]_T + nK_b[\mathrm{R}]_T\right)^2 - 4nK_b{}^2[\mathrm{R}]_T[\mathrm{L}]_T}\right] \quad (1)$$

where Q is the total heat content; V_c is the cell volume; and $[L]_T$ and $[R]_T$ are the total concentrations of the ligand (*APTES*) and receptor (*MNZ*) in the system, respectively.

Using K_b and ΔH°, the changes in Gibbs free energy (ΔG°) and entropy (ΔS°) can be calculated using Eqs. (2) and (3).

$$\Delta G^{\circ} = -RTlnK_b \quad (2)$$

$$\Delta G^{\circ} = \Delta H^{\circ} - T\Delta S^{\circ} \quad (3)$$

2.2.2. Synthesis of CdTe@TGA QDs

CdTe@TGA was synthesized using a one-pot method in an aqueous medium [41]. The synthesis was initiated using a mixture of 93.7 mg of $CdCl_2$ $7H_2O$ and 52.0 μL of the TGA surface ligand. Subsequently, a solution of NaOH (0.2 M) was added until a pH of 10 is obtained. Next, 5.2 mg of Na_2TeO_3 and 3.7 mg of the reducing agent $NaBH_4$ were added. The reaction temperature was maintained at 98 °C with magnetic stirring for 2 h in a glycerin bath. The QDs were purified using a non-solvent (acetone) through centrifugation at 3200 rpm for 10 min. The supernatant was discarded, and the material was dried in a vacuum oven at 60 °C for 24 h.

2.2.3. Synthesis of Fe3O4@TEOS MNPs

Magnetite MNPs were synthesized by modifying a coprecipitation method reported in the literature [42]. Initially, two 50 mL aqueous solutions containing 3.5 and 4.0 g of $FeSO_4$ and $FeCl_3$, respectively, were prepared and mixed together. The mixture was stirred with 25.0 mL of a solution of NaOH (10 M) in an inert atmosphere of nitrogen for 2 h and subsequently purified with water until a neutral pH is obtained. For the TEOS coating, 300.0 mg of Fe_3O_4 were dispersed in an isopropanol–water mixture (1:5 v/v), and then 5.0 mL of a solution containing 28% NH_4OH and 2.0 mL of TEOS (98%) were added. The reaction was maintained at room temperature with stirring for 12 h, followed by purification with deionized water until neutral pH. The particles were separated by the application of a magnetic field and dried in a vacuum oven at 60 °C for 24 h.

2.2.4. Preparation of MFMIP and MFNIP

The composite was synthesized in situ via the sol–silica gel method using the Stöber process [43] for molecular imprinting on the surface of nanoparticles. In a water–methanol mixture (1:1 v/v), 100 mg of MNZ was solubilized, followed by the addition of 547.0 μL of APTES and stirring for 1 h. A 10-milliliter aqueous dispersion containing 1.0 mg of CdTe@TGA and another 10-milliliter aqueous dispersions containing 240.0 mg of Fe_3O_4@TEOS were added to the reaction medium, followed by 2.08 mL of TEOS and 35.0 μL of NH_4OH. The molar ratio of the reagents MNZ, APTES, TEOS, and NH_4OH was 1:4:16:1.6 [44]. The synthesis was conducted for 22 h at room temperature, and the reaction mass was then washed with an acetic acid–methanol mixture (1:9) until the complete removal of MNZ molecules from the polymer matrix. MFNIPs followed the same synthetic route as MFMIPs, except for the use of MNZ. The composites were then dried at 60 °C in a vacuum oven for 24 h. Fig. 1 shows the steps for the synthesis of the composites.

2.3. Characterizations

2.3.1. Electron microscopy

The sizes and morphologies of the prepared materials were evaluated via scanning electron microscopy (SEM) using a Philips XL-30 microscope, Field Emission Gun (SEM-FEG), and the operating state of the equipment was at a voltage of 120 kV. Transmission electron microscopy (TEM) was performed on a Transmission Electron Microscope model FEI TECNAI G^2 F20 HRTEM.

2.3.2. Spectroscopic and surface characterizations

UV–vis and photoluminescence spectra (400–700 nm) were obtained using a Cambridge UV–vis spectrophotometer (CB40FJ, England) and a Varian Fluorescence spectrophotometer (Cary Eclypse, Australia), respectively. Fourier-transform infrared (FT-IR) spectra (4000–500 cm^{-1}) were obtained using a Shimadzu Infrared Spectrophotometer (A213749, Japan). Dynamic light scattering (DLS) and zeta potential (PZ) analyses were performed using a Zetasizer Nano ZS instrument (Malvern Instruments).

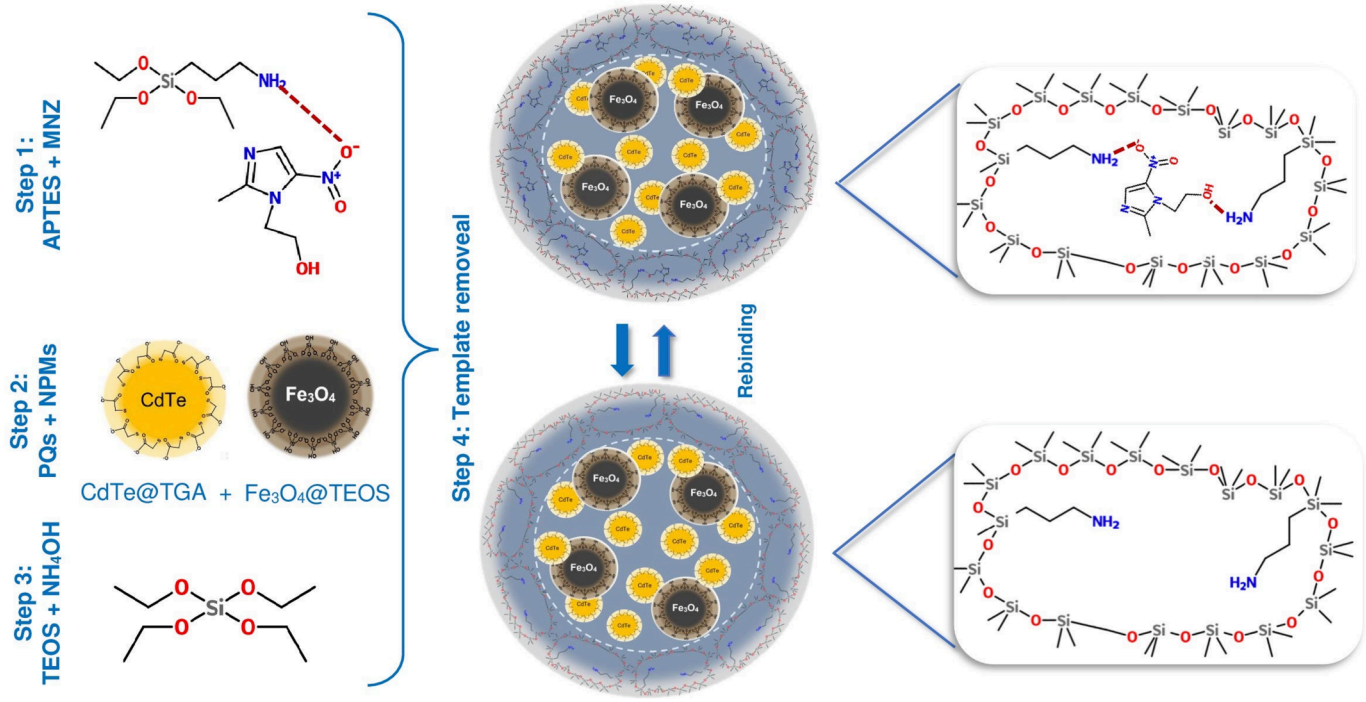

Fig. 1. Steps involved in the preparation of the printed MFMIP and non-printed MFNIP polymers.

2.3.3. Surface plasmon resonance (SPR) analysis

All SPR analyses to evaluate the interaction between the composites (MFMIP and MFNIP) with MNZ, SMX, and [Bmim]Cl were performed at 25 ℃ in a two-channel Biacore® X100 device (GE Healthcare, USA). Three CM5 sensor chips composed of carboxymethylated dextran covalently attached to a gold film were used as sensors. Two flow channels were present on the CM5 surface: the sample channel (in which MFMIP or MFNIP was immobilized) and reference channel (without composite immobilization). The SPR experiments were performed in triplicate to ensure accuracy, and the results were expressed as the means ± standard deviations (standard deviation was between 3 and 7%).

2.3.3.1. Immobilization of the composite on the chip surface. The composite (MFMIP or MFNIP) was immobilized on the surface of the CM5 sensor chip comprising the carboxymethylated dextran matrix via amide coupling [45]. The carboxylic acid groups were first activated for 7 min with a mixture of EDC (0.4 M) and NHS (0.1 M; 1:1 v/v) at a flow rate of 10 μL min^{-1}. A suspension of 30 μg mL^{-1} of the composite (MFMIP or MFNIP) in 10 mmol/L of sodium acetate (pH 4) was then injected over 7 min, resulting in a low-density composite immobilization (1972 RU for MFMIP and 2168 RU for MFNIP) that minimized potential mass transport and agglomeration effects on the sensorgram data. Finally, excess activated carboxyl groups were blocked with ethanolamine for 7 min. To monitor possible non-specific interactions between the composite and chip surface, a reference channel was prepared as previously described, but without composite immobilization.

2.3.3.2. Analysis of MNZ interactions with the immobilized composite. Interactions between the composites (MFMIP or MFNIP) and MNZ and between MFMIP and SMX or [Bmim]Cl were evaluated under conditions of pH 7.4 (HBS-P buffer, 0.01 M HEPES, 0.15 M NaCl, and 0.05% v/v surfactant P20) for various concentrations of the analytes (MNZ, SMX, or [Bmim]Cl) ranging 0.4–1.8 mM. The buffer was injected before each composite–analyte binding cycle to obtain a baseline. The analyte solutions were then injected into the sample and reference channels of the chip over 60 s at a flow rate of 10 μL min^{-1}. Subsequently, the pure buffer was injected again into both sensor chip channels to dissociate the formed complexes. Finally, flowing buffer was injected twice over 360 s at a flow rate of 10 μL min^{-1} to regenerate the chip surface at the end of each experiment. The reference and sample channel signals were subtracted, and the net SPR signals (resonance units, RU) were traced over time (sensorgrams).

2.3.3.3. Kinetic studies on composite–MNZ interactions. The binding model proposed by Schasfoort (2017) was used to determine the kinetic parameters of association (k_a) and dissociation (k_d) while studying the interactions between the immobilized composites (MFMIP or MFNIP) and various analytes (MNZ, SMX, and [Bmim]Cl).

The sensorgrams obtained for the interactional studies were mathematically treated according to global adjustments made using integrated rate Eqs. (4) and (5) to determine the values of the observed constants (k_{obs}) and dissociation parameters (k_d) for the evaluated processes. The k_a values were determined via the slopes (Eq. (6) of the k_{obs} vs. MNZ concentration curves (Figure S11).

$$RU(t) = RU_{\max(t_\infty)}\left[1 - e^{-k_{obs}(t-t_0)}\right] \tag{4}$$

$$RU(t) = RU(tm)e^{-k_d(t-t_m)} \tag{5}$$

and

$$k_{obs} = k_a{}^*[analyte] + k_d \tag{6}$$

where RU(t), $RU_{\max}$, and $RU(tm)$ denote the SPR response at time t, SPR signal at the beginning of the descending exponential curve of the sensorgram, and SPR response of the analyte (MNZ, SMX, or [Bmim]Cl) under the composite saturation condition, respectively.

The activation energy ($E_x^{\ddagger}$) associated with the formation of the $[\text{composite (MFMIP or MFNIP)} - \text{MNZ}]^{\ddagger}$ transition complex can be determined by evaluating the dependence of $\ln k_a$ and $\ln k_d$ on temperature, using a non-linear Arrhenius fit (Eqs. (7) and (8). In this approach, the transition complex is assumed to have been formed either from the association of free materials, composites and MNZ ($E_a^{\ddagger}$) or dissociation of the thermodynamically stable complex ($E_d^{\ddagger}$); [46].

$$lnk_x = a + b\left(\frac{1}{T}\right) + c\left(\frac{1}{T}\right)^2 + d\left(\frac{1}{T}\right)^3 \tag{7}$$

and

$$E_x^{\ddagger} = -R\left[b + 2c\left(\frac{1}{T}\right) + 3d\left(\frac{1}{T}\right)^2\right] \tag{8}$$

where b, c, and d are constants graphically determined via polynomial adjustment, k_x corresponds to k_a (x = a) or k_d (x = d), R is the universal gas constant (8.314 J mol^{-1} K), and T is the temperature in K.

The Eyring equation was used to determine the change in Gibbs free energy of activation ($\Delta G_x^{\ddagger}$; Eq. (9), and the changes in enthalpy of activation ($\Delta H_x^{\ddagger}$) and entropy of activation ($\Delta S_x^{\ddagger}$) were determined using Eqs. (10) and (11), respectively, [47,48].

$$k_x = \frac{k_B T}{h} exp\left(\frac{-\Delta G_x^{\ddagger}}{RT}\right) \tag{9}$$

$$\Delta H_x^{\ddagger}(T) = E_{act(x)}(T) - RT \tag{10}$$

and

$$T\Delta S_x^{\ddagger}(T) = \Delta H_x^{\ddagger}(T) - \Delta S_x^{\ddagger}(T) \tag{11}$$

where k_B is the Boltzmann constant, and h is the Planck constant.

2.4. Adsorption kinetics studies

To evaluate the adsorption kinetics of MNZ, 30 uM of the analyte were added to 0.2 mg mL^{-1} of the MIP composite. Fluorimeter readings were obtained from 1 to 120 min. The concentration of the analyte was calculated using the emission intensity and the calibration curve developed for the MIP, wherein the amount of MNZ adsorbed in the matrix and that left in the supernatant could be defined, because the initial concentration was known. The adsorption capacities of the Q composites were determined using the following relationship:

$$Q = \frac{(C_0 - C_1)V}{m} \tag{12}$$

where C_0, C_1, V, and m represent the initial concentration of the MNZ solution (mg L^{-1}), concentration of MNZ in the supernatant after adsorption (mg L^{-1}), initial volume of the MNZ solution (L), and mass of the composite (g), respectively.

2.5. Sensitivity and selectivity tests

In a pilot test, the MFMIPs and MFNIPs were evaluated for their sensitivities to various concentrations of MNZ in water, using spectrofluorimetry. For this, 50 mg of each material were dispersed in 10.0 mL of water and placed in an ultrasound bath for 15 min. An aliquot of this suspension (200 μL) was then added to 5 mL of seven solutions (pH 6.0) containing MNZ at concentrations ranging 1–60 μM. The fluorescence spectrum of each concentration was obtained at wavelengths between 400 and 800 nm, with an excitation wavelength of 340 nm and a resolution of 5 nm. The experiment was performed in triplicate. The lower

limit of detection (LOD) and lower limit of quantification (LOQ) were obtained using Eqs. (13) and (14), where, a is the slope of the straight line of the MNZ concentration (μM) as a function of the emission intensity (a.u.), and $SD_{reference}$ is the standard deviation of the response for ten measurements of a reference sample.

$$LOD = \frac{3 \times SD_{reference}}{a} \quad (13)$$

$$LOQ = \frac{10 \times SD_{reference}}{a} \quad (14)$$

The selectivities of the sensors prepared for the detection of MNZ were evaluated by comparing the detection capacity of the composites against two interferents: sulfametroxazole (SMX) and butylmethylimidazolium chloride ([Bmim]Cl). The same masses of MFMIP and MFNIP used in the sensitivity test were used in the selectivity test, and the concentration of the MNZ, SMX, and [Bmim]Cl solutions was 30 μM (pH 6.0). The results obtained for MFNIP and MFMIP were compared to assess the influence of the cavities on sensor selectivity.

3. Results and discussion

3.1. Rational planning, preparation, and characterizations of materials

3.1.1. Isothermal titration calorimetry (ITC) analysis

ITC is a quantitative technique commonly used to determine thermodynamic parameters related to biochemical interactions in solutions [49,50]. Although there are few reports in the literature about using ITC to determine the binding affinity of MIPs for small molecules [51] and to predict the optimum ratio of model molecules to functional monomers [52,53], ITC provides energetics data and fundamental insights into the binding mechanisms of MIPs. Therefore, to evaluate the number of template molecules (MNZ) bound per monomer (APTES) for the formation of selective cavities and the energy involved in this interaction during the molecular imprinting process, the binding of APTES to MNZ was investigated using ITC. Thus, the equilibrium binding constant (K_b), standard enthalpy changes (ΔH°), and complex stoichiometry (n) were obtained directly via a single experiment.

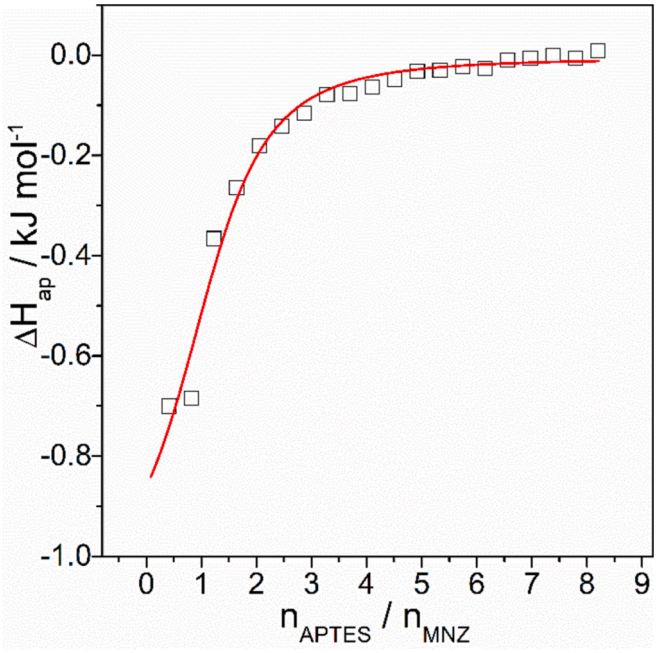

Fig. 2. Plot of ΔH_{ap} *versus* molar ratio for the MNZ–APTES interaction. The data points reflect the experimental injection heat after correction for the heat of dilution, while the solid line represents the calculated fit of the data.

Fig. 2 shows the plot of the apparent molar enthalpy change ($\Delta H_{app-int}$) of MNZ–APTES binding against the molar ratio (n_{APTES}/n_{MNZ}), which was obtained at 298.15 K.

By fitting the ΔH_{ap} *versus* molar ratio curves to the SSIS model [40] described by Eq. (1), K_b, n, and ΔH°_{cal} were calculated. Using these parameters, the ΔG^{o} (Eq. (2) and $T\Delta S^{o}$ (Eq. (3) values for the MNZ–APTES complex formation were determined. The K_b and n values obtained using ITC were 2.575 × 10^3 L mol^{-1} and 1.162, respectively, indicating that approximately 1 mol of APTES was bound to 1 mol of MNZ. Using the K_b value determined here, a negative ΔG° value (−19.468 kJ mol^{-1}) was obtained for the MNZ–APTES interaction. The negative value indicates the predominance of the MNZ–APTES complex over free molecules during thermodynamic equilibrium and results mainly from the contributions of three molecular processes that occur in the system: the desolvation of MNZ and APTES molecules, intermolecular interaction between them, and conformational changes in the structures of the model molecule and monomer, owing to their interaction. Therefore, to determine the driving force involved in the formation of the MNZ–APTES complex, their enthalpic and entropic contributions were analyzed.

The formation of a complex between MNZ and APTES resulted in a decrease in the enthalpy (ΔH° = −1.079 kJ mol^{-1}) and an increase in the entropy ($T\Delta S^{\circ}$ = 18.389 kJ mol^{-1}) of the system. A negative ΔH° value indicates that hydrogen bonds between the amino functional group present in APTES and the nitro and hydroxyl groups of MNZ dominated complex formation. Therefore, although other processes occurring in the system also led to an increase in enthalpy (e.g., desolvation of MNZ and APTES molecules and conformational changes in the interacting molecules), they were overcome by the energy released during the MNZ–APTES interaction process. However, the entropic gain could be explained by the increase in the degrees of freedom of the water molecules released from the solvation layers of MNZ and APTES during complex formation.

Subsequently, the composite was prepared using the ideal molar proportions of the model molecule and monomer. Because the added monomer was not expected to interact effectively with the model molecule (MNZ) in the MFMIP preparation, a higher molar ratio was used, that is, (MNZ)/(APTES) = 1:4.

3.1.2. Syntheses and characterizations of the composites

The MFMIPs and MFNIPs were obtained from in-situ polymerization processes, which occurred on the surfaces of CdTe@TGA and Fe_3O_4@-TEOS, via the sol–gel method. Hydrogen-bonding interactions between MNZ and the polymeric matrices were favored by the hydroxyl and amine groups present in the APTES functional monomer. The final composites exhibited MNZ recognition, extraction, and quantification abilities in aqueous matrices.

In the infrared spectra shown in Fig. S2a (Supplementary Material), the TGA coating on the CdTe QDs was confirmed by a modification in the bands of pure TGA. For example, the S–H stretching band was not observed, indicating interactions between sulfur and the PQ surface. Furthermore, the stretching band of the C=O group shifted from 1693 cm^{-1} to a shorter absorption wavelength of 1536 cm^{-1}, indicating that carboxylic acid had been transformed into a carboxylate anion [54]. The MNPs had also been effectively coated with TEOS, because in the spectra of the magnetite nanoparticles coated with TEOS (Fig. S2b, Supplementary Material), intense absorption bands were observed at 1085, 956, and 802 cm^{-1}, which were attributed to the stretching vibrations of Si–OH groups and bending vibrations of Si–CH_2 and Si–CH_3 groups. However, the bands corresponding to Si–OH and Si–O–Si vibrations may have been overlaid, possibly because of the coating process, the formation of Si–O–Si and Si–OH bonds, and the proximity of the absorption wavelengths of the vibrations of these bonds to those of the bending vibrations of the Si–CH_2 and Si–CH_3 bonds, respectively [55]. The FT-IR spectra of TEOS, MFMIP, and MFNIP (Fig. 3) suggest that the Fe_3O_4

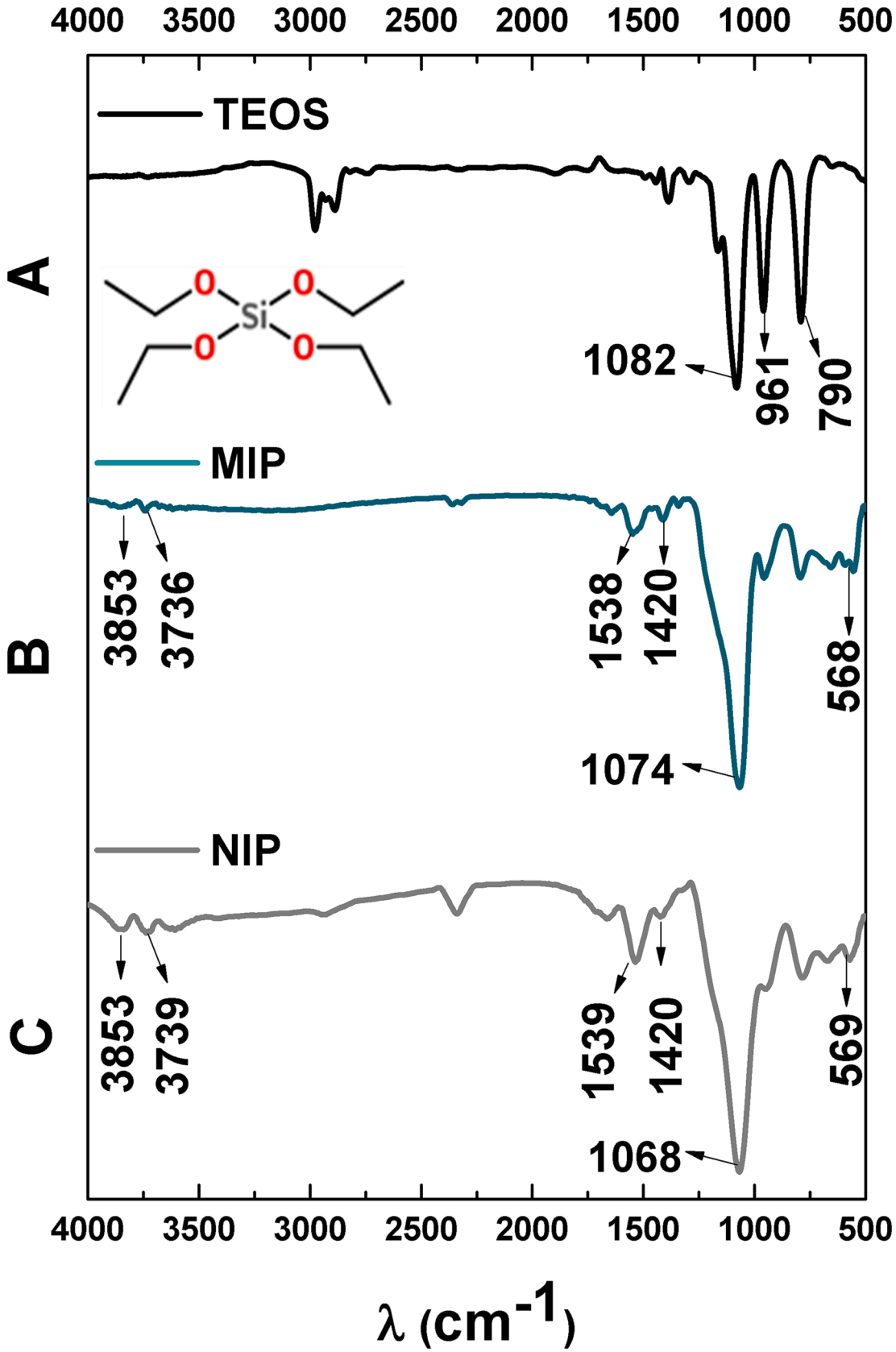

Fig. 3. FT-IR spectra for A) TEOS, B) MIP, and C) NIP.

nanoparticles were successfully coated with TEOS and demonstrate evidence of polymerization on the NP surfaces.

The infrared-region absorption spectrum of TEOS is as shown in Fig. 3A. The main absorption bands at 1082, 967, and 790 cm^{-1} were attributable to the stretching vibrations of the Si–O bond and the bending vibrations of the Si–CH_2 and Si–CH_3 groups, respectively. Similar bands were observed in the spectra of MIP and NIP (Fig. 3B and 3C). However, as a result of polymerization, Si–O–Si bonds were formed, which absorb at wavelengths close to those of the Si–CH_3 bending vibrations. Therefore, the Si–O–Si bands may have overlapped with those of Si–CH_3 in the spectra of MFMIP and MFNIP, with absorptions at 791 and 782 cm^{-1}, respectively [55]. Furthermore, two other bands in the spectrum of MIP, with absorptions at 3858 and 3736 cm^{-1}, and in the spectrum of NIP, with absorptions at 3853 and 3739 cm^{-1}, were attributed to the symmetric and asymmetric stretching vibrations of the amino groups (NH_2) close to the electronegative atoms. These bands originated from the functional monomer APTES, which had been used in the first step of the synthesis of the MFMIPs and MFNIPs for the generation of specific template cavities [16].

The difference in the absorption intensities of the MFMIP and MFNIP spectra, mainly the absorption bands of the amino groups, was notable. This difference may have been a consequence of variations in the positions of the functional groups, which may have been located at the surface or the interior of the polymer matrix, owing to the presence of the template during the synthesis of the material.

Some bands appeared in Fig. 3A in the region below 700 cm^{-1}, which were attributed to the stretching vibrations of the Fe–O bonds, indicating the presence of the magnetic nanoparticles that had been used in the synthesis of the composites [23]. The presence of CdTe@TGA quantum dots in the polymer matrix was also confirmed by the presence of two nearly overlapping bands in the spectra of Fig. 3B and 3C, which were similar to those observed for the nanocrystals in their infrared spectrum (Fig. S2a). In the spectrum of the QDs, these bands appeared at wavelengths of 1536 and 1358 cm^{-1}, whereas in the spectra of the MFMIPs and NIPs, they appeared at 1538 and 1420 cm^{-1} (Fig. 3B) and 1539 and 1420 cm^{-1} (Fig. 3C), respectively, which corresponded to the symmetrical and asymmetrical stretching vibrations of the carboxylate ions present on the surface of the QDs [54]. These results confirm the success of the sol–gel synthesis during the surface polymerization of QDs and MNP@TEOS.

The morphologies of CdTe@TGA, Fe_3O_4@TEOS, and the composites were studied using transmission electron microscopy (TEM) and scanning electron microscopy (SEM), the results of which are shown in Fig. 4, and more details are shown in Figures S4, S5, and S6 (Supplementary Material). Fig. 4a shows a histogram of the size distribution, indicating that the synthesized QDs were spherical, monodisperse crystals with an average diameter of 3.1 nm. The HRTEM image in Fig. 4b shows that the Fe_3O_4@TEOS NPs were spherical and exhibited a slightly higher

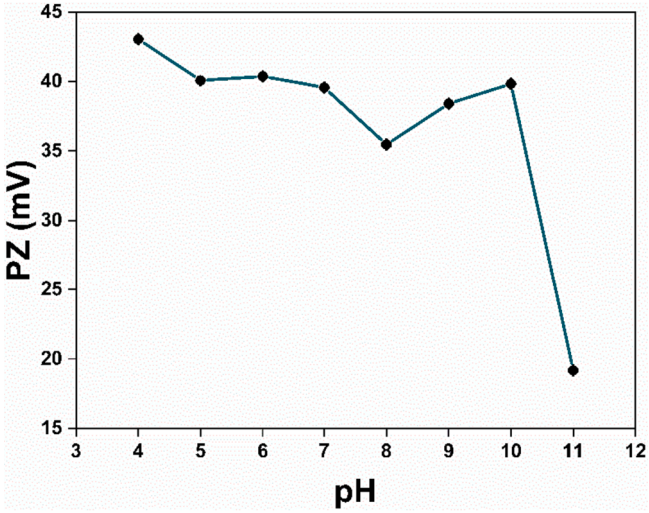

Fig. 5. Influence of pH on the zeta potential of MFMIP. The error bar of each measurement was smaller than the sizes of the symbols used.

polydispersity than the Fe_3O_4 NPs. The histogram of Fe_3O_4@TEOS showed a diameter of 18.4 ± 3.6 nm, averaging approximately 7 nm more than that of the Fe_3O_4 NPs before coating, indicating that the NPs were coated with silica.

Fig. 5 shows the zeta potential (PZ) curve for MFMIP, which indicates that variations in pH caused the PZ to remain practically constant up to pH 10. The variations in PZ were in the modulus of 10 mV, yet the values remained in the modulus greater than 30 mV. A pH of 6 was selected for all experiments involving the composites (imprinted and non-printed), because this value can be easily adjusted for aqueous media, wherein the molecular structure of MNZ (pKa = 2.62) is deprotonated, which favors the interaction of the composite analyte.

In addition, the stability of the MFMIPs containing the CdTe QDs can be affected by pH. A study by Xu et al. [56] demonstrated that the fluorescence intensities of MFMIPs with CdTe probes, studied at pH values from 2 to 14, decreased at pH values below 4 or above 12, indicating that the imprinted silica shell was ionized at these pH values, which affected the stability of both the QDs and cavities [56]. Therefore, a pH closer to neutral was chosen.

3.2. Kinetic composite–MNZ interaction study via SPR

Although molecular imprinting technology has been recurrently investigated for the detection of antibiotics, rational planning and knowledge on specific interactions are still scarce, which limits advancements in the use of nanocomposites [57,58]. Therefore, we

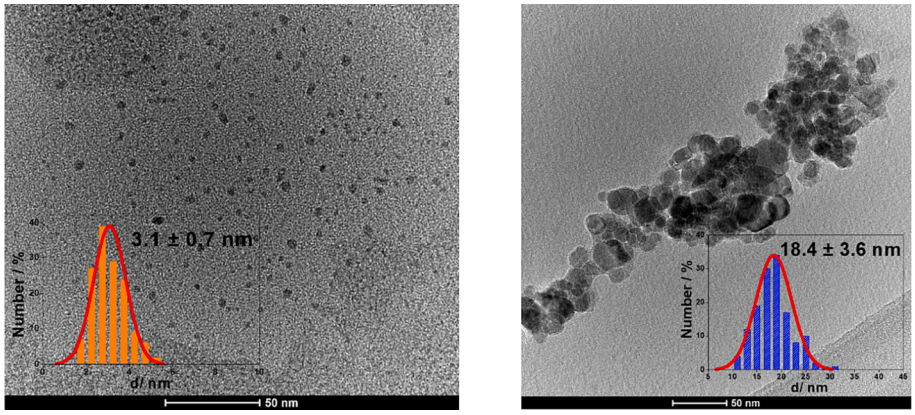

Fig. 4. HRTEM images for: (a) CdTe quantum dots and (b) Fe_3O_4@TEOS, both with insets showing size distribution histograms.

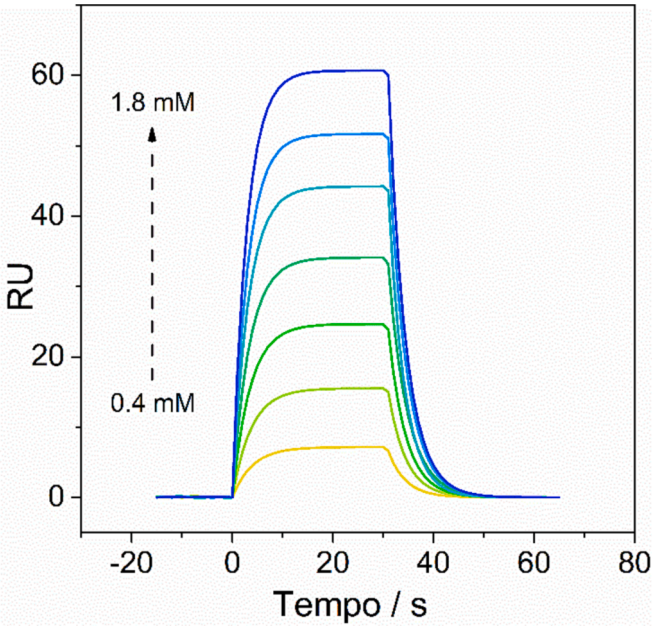

Fig. 6. SPR sensorgrams for the complex formation between the immobilized MFMIP (1972 RU) and various concentrations of MNZ (0.4–1.8 mM) at 298.15 K.

assessed the recognition properties of the composite–MNZ interaction via SPR binding studies, which resulted in the sensorgrams shown in Fig. 6.

As shown in Fig. 6 (298.15 K) and Figure S10 (285.15–301.15 K), various concentrations of MNZ (0.4–1.8 mM) were flowed over the chip surface with immobilized MFMIP, resulting in seven binding curves. At each cycle, which is called a sensorgram, the buffer solution was first injected over the surface to define the baseline, followed by the injection of the MNZ solution. As the MFMIP and MNZ bonded, the concentration of the complex gradually increased, as indicated by an increase in RU, until a steady state was reached. Finally, the buffer was injected once more to induce the dissociation of the thermodynamically stable complexes ([MFMIP–MNZ]°).

The imprinting effect on the sensitivity of the composite was evaluated via SPR experiments with a chip containing immobilized MFNIP. As shown in Figure S13, a low RU signal indicated that no interaction occurred between MFNIP and MNZ. This shows that the presence of imprinted sites with sizes and shapes complementary to the template molecule is fundamental to the molecular recognition of nanocomposites.

The selectivities of the imprinted sites were also studied using two molecules with chemical structures similar to (C_4mimCl) and different from (SMX) those of MNZ. The obtained sensorgrams (Figures S12 and S13) showed very low RU signals for MFMIP in the presence of either C_4mimCl or SMX. This indicates that, in addition to shape and size complementarity, the specific interactions between the template molecule and the imprinted site result in a high selectivity of the nanocomposite towards MNZ.

By globally fitting the sensorgrams (Fig. 6 and Figure S10) to the 1:1 Langmuir binding model [59] which best fitted the data, the kinetics of the interaction between MFMIP and MNZ were determined. As the analyte and buffer were injected continuously, the concentration of MNZ in the flow cell was maintained over time. Thus, the association phase could be described by a pseudo-first-order rate law, which contained information regarding the association (k_a) and dissociation (k_d) kinetic constants (Eqs. (4) and (6). In contrast, the dissociation phase was described by a first-order rate law, which contained information on k_d only (Eq. (5). Table 1 lists the values of k_a and k_d obtained at various temperatures.

Table 1
Values of k_a and k_d for the complex formation between MFMIP and MNZ at various temperatures.

T/ K	k_a*/10^2 M^{-1} s^{-1}	k_d*/ s^{-1}
285.15	0.75	0.45
289.15	0.54	0.43
293.15	0.63	0.43
297.15	0.90	0.44
298.15	1.04	0.44
301.15	1.48	0.45

*For all parameters, the standard deviation was less than 4%.

k_a and k_d were in the order of 10^2 $M^{-1}s^{-1}$ and 10^{-1} s^{-1}, respectively, and their values indicated that, on an average, 89 complexes were formed per second, whereas 44% of them dissociated during the same time interval. In the preparation of the MFMIP, after the interaction of the monomer (APTES) with the template molecule, TEOS is added to form a crosslinked rigid polymer with a cavity that maintains its shape even after the template molecule is washed away [60]. Therefore, the slow association between free MNZ and MFMIP may be indicating that, even though MFMIP have a rigid structure, conformational changes occurs in the 3-aminopropyl groups inside the cavity for [MFMIP–MNZ]° to be formed.

To better understand the dynamics of composite–MNZ recognition, the energetic parameters of activation were determined according to transition state theory [61]. The activation energies ($E_x^{\ddagger}$) were obtained using Eqs. (7) and (8), via the non-linear regression of the ln k_x vs. 1/T curves (Figure S12), while the changes in the free Gibbs energy ($\Delta G_x^{\ddagger}$), enthalpy ($\Delta H_x^{\ddagger}$), and entropy ($\Delta S_x^{\ddagger}$) of activation were calculated using Eqs. (9)–(11), where × = a corresponds to association and × = d corresponds to dissociation. Fig. 7 shows the dependence of these parameters on temperature.

$\Delta G_a^{\ddagger}$ and $\Delta G_d^{\ddagger}$ were associated with the potential energy and configurational/conformational barriers that separated the intermediary state from free MNZ, MFMIP, and [MFMIP–MNZ]°, respectively. In the investigated temperature range, both $\Delta G_a^{\ddagger}$ and $\Delta G_d^{\ddagger}$ values were positive and remained almost constant, indicating a compensation between the values of $\Delta H_x^{\ddagger}$ and $T\Delta S_x^{\ddagger}$ with increasing temperature, as verified by the curves shown in Fig. 8.

The formation of [MFMIP–MNZ]‡, either via the association of free MNZ and MFMIP or the dissociation of [MFMIP–MNZ]°, occurred with a linear dependence of $\Delta H_x^{\ddagger}$ on the $T\Delta S_x^{\ddagger}$ values with increasing temperature. This may have been caused by the modification of the solvation structure of the interacting entities during the formation of an activated complex or an induced fit of the binding site where the interaction occurred [62].

When the template molecule reached the binding cavity to form the activated complex, water molecules in the MNZ solvation layer and imprinted sites were released to the bulk, which resulted in an increase in the enthalpy and entropy (I) of the system. MNZ then bonded with the nanocomposite via hydrogen bonding with the amine groups present in the imprinted site, losing configurational degrees of freedom, which resulted in a decrease in enthalpy and entropy (II). In addition, during the formation of the activated complex, an induced fit of the binding site, which is generally accompanied by an increase in enthalpy and entropy (III), may have occurred.

For the formation of [MFMIP–MNZ]‡, besides the shape-recognition, the 3-aminopropyl groups pointing inward the cavity must be in the right orientation to perform the hydrogen bonding with MNZ. Considering the temperature dependence of the processes I, II, and III, the negative $E_a^{\ddagger}$, $\Delta H_a^{\ddagger}$, and $T\Delta S_a^{\ddagger}$ values observed at low temperatures can be attributed to the 3-aminopropyl groups having less rotational degrees of freedom and, probably, remaining in a conformation that favors the

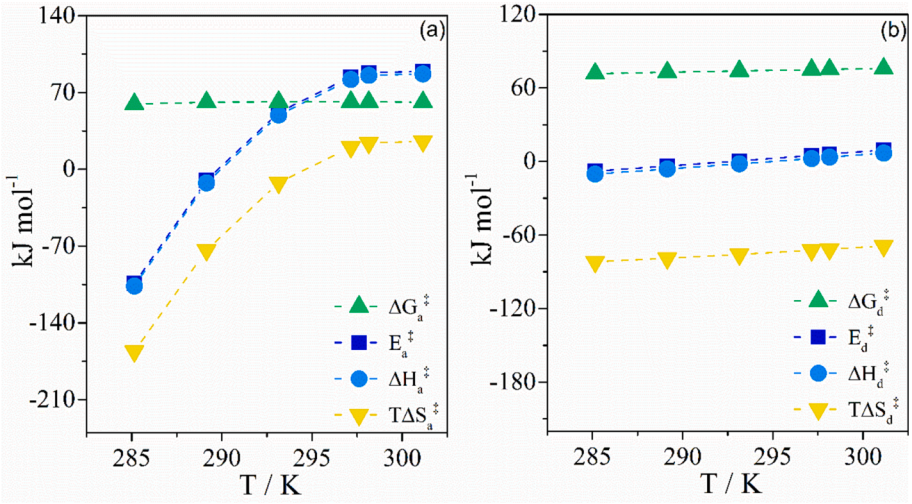

Fig. 7. Dependence of the energetic parameters of activation on temperature for the formation of the transition complex ([MFMIP–MNZ]‡) from the association (a) and dissociation (b) phases. The error bar of each measurement was smaller than the sizes of the symbols used.

hydrogen bonding with the MNZ molecule. Therefore, the energy release and entropy decrease coming from process II, overcame processes I and III.

However, as the temperature increased, $E_a^{\ddagger}$, $\Delta H_a^{\ddagger}$, and $T\Delta S_a^{\ddagger}$ also increased becoming positive. Although the cavity remains rigid as the temperature of the system is increased, the 3-aminopropyl groups gain rotational degrees of freedom. The more flexible the 3-aminopropyl groups, the more hindered the formation of hydrogen bonding with MNZ due to the different orientations assumed by these groups. Consequently, the energetic and entropic contributions from process II decrease, and the energy release and entropy increase from the desolvation of the molecules (I) and the induced fit of the binding site (III) dominate the values of $E_a^{\ddagger}$, $\Delta H_a^{\ddagger}$, and $T\Delta S_a^{\ddagger}$.

In contrast, the formation of [MFMIP–MNZ]‡ via the dissociation of [MFMIP–MNZ]° occurred with very small $E_a^{\ddagger}$ and $\Delta H_a^{\ddagger}$ values and negative $T\Delta S_a^{\ddagger}$ throughout the studied temperature range. Because the desolvation of the cavity and the MNZ molecule do not occur in this step, this result indicates a restructuration of the complex in which: (a) the energy absorbed and released from breaking and forming intermolecular interactions due to changes in the conformation of the complex are counterbalanced; and (b) the complex becomes more structured when it dissociates from [MFMIP–MNZ]° to [MFMIP–MNZ]‡ as shown by the decrease of the entropy.

The analysis of the association and dissociation steps thus revels that when the free MNZ associates with the MFMIP through hydrogen bonding, a lower entropy state is reached with the formation of [MFMIP–MNZ]‡. Then, the relaxation of the complex occurs with the increase of the system's entropy until [MFMIP–MNZ]° is finally formed.

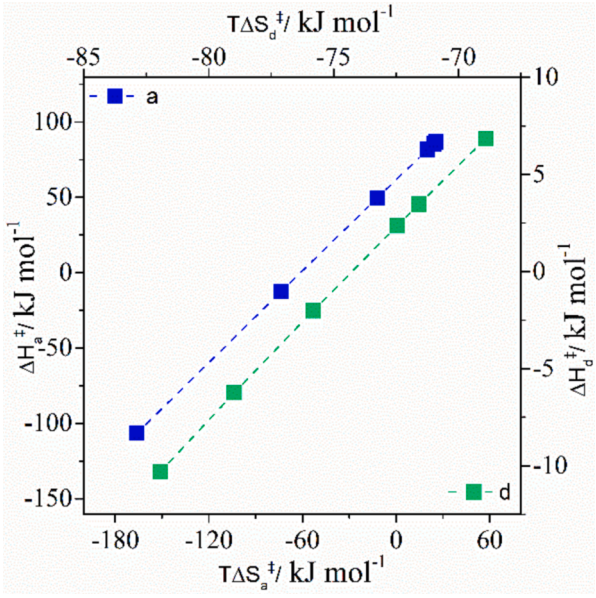

Fig. 8. Plots of $\Delta H_x^{\ddagger}$ *versus* $T\Delta S_x^{\ddagger}$ for the [MFMIP–MNZ]‡ formation via the association between the MFMIP–MNZ and MNZ species (x = a) or [MFMIP–MNZ]° dissociation (x = d). The error bar of each measurement was smaller than the sizes of the symbols used.

3.3. Adsorption kinetics

The adsorption of MNZ on the MFMIP was studied from 0 to 600 min. Fig. 9 shows the change in the concentration of the analyte in the matrix over time. The adsorption process can be divided into two steps: fast and slow. At 0 min, MNZ was absent in the polymeric matrix. Upon contact, MNZ was rapidly adsorbed; in the first minute, 82.63% of the mass of MNZ initially added had already been adsorbed by the composite. Then, a slower adsorption process followed, starting at 1 min, which led to equilibrium.

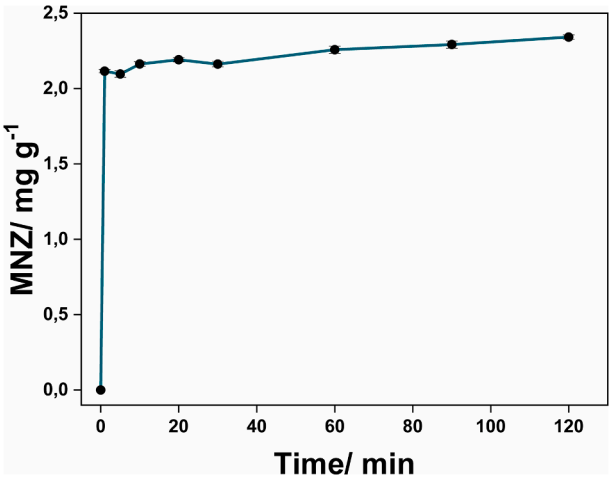

Fig. 9. Rate of adsorption of MNZ by the MFMIP. The error bar of each measurement was smaller than the sizes of the symbols used.

3.4. Sensitivity tests

The influence of agitation on the interaction between MNZ and the composite was first investigated. A previous evaluation had indicated that agitation prevented fluorescence quenching in MNZ–composite (MFMIP or MFNIP), whereas without agitation, fluorescence was immediately suppressed after the contact of MNZ with the composite. Therefore, for the MNZ–composite interaction tests, agitation was not employed, which was consistent with the methodologies reported in the literature for MFMIPs containing QD fluorescent probes [63].

Sensitivity tests were used to evaluate the sensitivities of the MFMIPs and MFNIPs for the detection of various concentrations of MNZ. MFMIP suspensions (0.2 mg mL^{-1}) prepared using 1–60 μM MNZ were tested. Fig. 10 shows the fluorescence quenching for both composites, with a high linear correlation as the MNZ concentration increased. The results indicate LODs of 1.28 and 2.81 μM and LOQs of 5.00 and 10.00 μM for the MFMIP (Fig. 10a) and MFNIP (Fig. 10b), respectively. Thus, the influence of the selective cavities present in the MFMIP was evident, which was twice that observed in the interaction between MNZ and MFNIP.

The stability and reproducibility of the sensor can be assessed by calculating the relative standard deviation (RSD%) derived from triplicate sample analyses with identical concentrations during the metronidazole sensitivity test. The RSD% values ranged from 0.130% to 1.25% for NIP and from 0.274% to 1.72% for MIP across all analyses. These results demonstrate that the sensor exhibits both reproducibility and stability.

3.5. Sensor selectivity

In the selectivity studies, 30 μM of each molecule were used, and the results are shown in Fig. 11.

These results demonstrated that MFMIP was more selective for MNZ than MFNIP. The MFNIP sensor exhibited fluorescence quenching for all molecules tested, whereas the MFMIP sensor exhibited a significant fluorescence suppression only in the presence of MNZ, which was the template molecule. Thus, the formation of selective cavities with specific chemical groups that can interact with MNZ can significantly reduce the matrix interference effect [3].

A comparison of the quenching effects of the contact of MFMIP with SMX, [Bmim]Cl, and MNZ indicated 4.2%, 3.3%, and 41.34% decrease in fluorescence, respectively. This indicated that selective cavities were formed in the MFMIP that favored interaction with MNZ, possibly via hydrogen bonding, and promoted selective suppression [63].

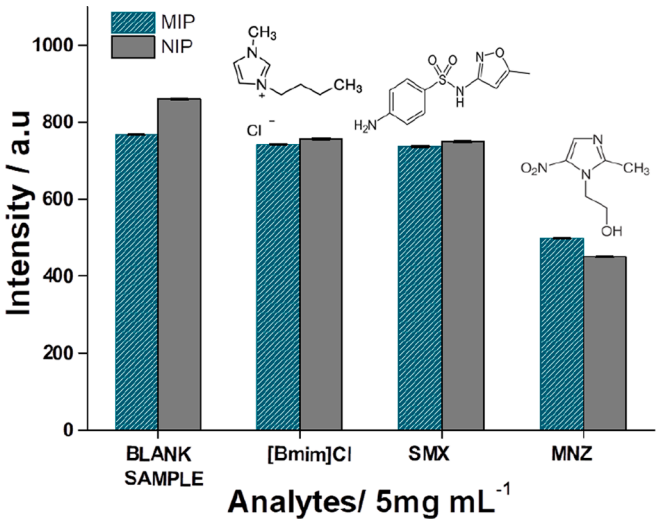

Fig. 11. Emission intensities of the MFMIP and MFNIP composites in the presence of various analytes.

4. Conclusions

In this study, we successfully synthesized CdTe quantum dots (QDs) and Fe_3O_4 magnetic nanoparticles (MNPs) embedded in a molecularly imprinted polymer matrix to create a metronidazole (MNZ)-selective sensor, termed MFMIP. Our sensor exhibited excellent performance and selectivity in detecting MNZ in water samples, with a low limit of detection (LOD) of 1.28 μM and a linear range of 5–60 μM. The MFMIP sensor outperformed the non-imprinted reference composite (MFNIP) in terms of sensitivity, making it a promising candidate for real-time MNZ analysis without the need for complex sample preparation.

Through SPR studies, we confirmed the highly specific interactions between MFMIP and MNZ, elucidating the kinetic aspects of their binding. The MFMIP-MNZ binding mechanism involved a hydrogen bonding process leading to the formation of $[MFMIP\text{-}MNZ]^{\ddagger}$, followed by the relaxation of the transition complex and the final $[MFMIP\text{-}MNZ]^{\circ}$ formation. This detailed understanding of the interaction enhances our confidence in the reliability and accuracy of the MFMIP sensor.

Notably, our MFMIP sensor demonstrated superior selectivity for MNZ over other analytes with similar and different chemical structures, including sulfamethoxazole (SMX) and 1-butyl-3-methylimidazolium chloride ([Bmim]Cl). This selectivity, coupled with the ease of

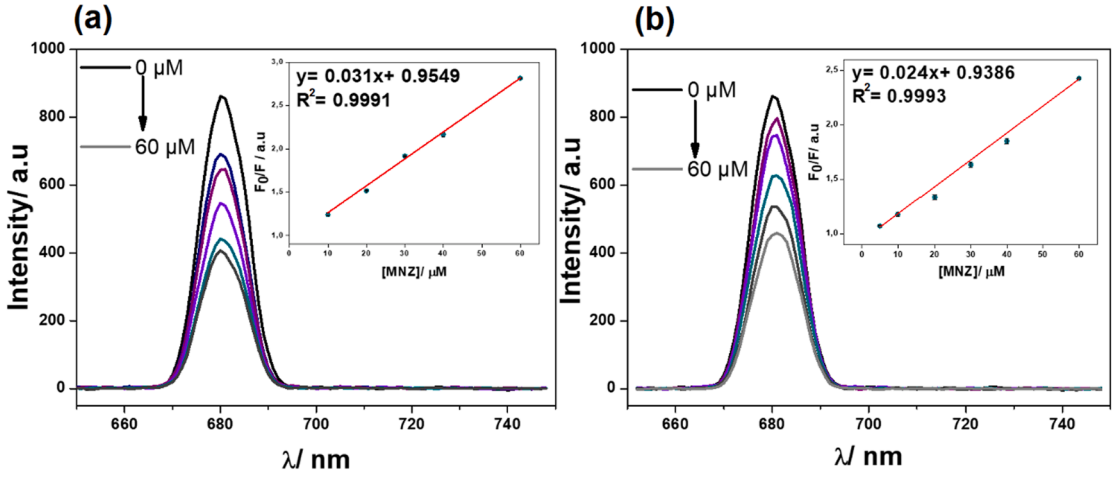

Fig. 10. Photoluminescence spectra of a) MFMIP and b) MFNIP during the sensitivity tests for MNZ. The error bar of each measurement was smaller than the sizes of the symbols used.

handling and rapid analysis capability of the MFMIP sensor during the first minute of contact with the analyte, sets it apart from current MNZ detection methods.

In conclusion, our work presents a novel and efficient MNZ sensor with great potential for trace-level MNZ detection in environmental and clinical applications. The successful integration of quantum dots and magnetic nanoparticles into the molecularly imprinted polymer matrix highlights the versatility and effectiveness of this approach for developing highly sensitive and selective sensors. Future research can explore the applicability of this sensor in real-world scenarios, offering a valuable tool for monitoring MNZ concentrations in various settings.

Funding

This work was supported by the *Conselho Nacional de Desenvolvimento Científico e Tecnológico* (CNPq), *Fundação de Amparo à Pesquisa do Estado de Minas Gerais* (FAPEMIG), and *Coordenação de Aperfeiçoamento de Pessoal de Nível Superior* (CAPES) – Financing Code 001.

Declaration of Competing Interest

The authors declare that they have no known competing financial interests or personal relationships that could have appeared to influence the work reported in this paper.

Data availability

The authors are unable or have chosen not to specify which data has been used.

Acknowledgments

The authors would like to thank Universidade Federal de Alfenas (UNIFAL-MG) making their facilities available.

Author contributions

Laís Mendes Alvarenga performed the synthesis, purification, and characterization of CdTe QDs, MNP, and MFMIP/MFNIP, participated in the interpretation of the SPR data, and contributed to the article writing. Cristiane Feliciano performed the synthesis, purification, and characterization of CdTe QDs and MFMIP/MFNIP. Bruno Giordano Alvarenga participated in the analysis and interpretation of the ITC data. Hauster Maximiler Campos de Paula performed the SPR experiment. Yara Luiza Coelho participated in the study and interpretation of the SPR data, contributed to the article writing, and preparation of the work. Luis Henrique Mendes da Silva participated in designing the research with the SPR technique, led the analysis and discussion of the SPR data, and participated in the article writing. Luiz Fernando Gorup used electron microscopy techniques to characterize the different nanoparticles and nanostructures in this work. Mariane Gonçalves Santos participated in the planning of the construction of the MIPs and contributed to the writing and revision of the final text of the manuscript. Luciano Sindra Virtuoso participated in the design of the research, interpretation of the data, and article writing.

Appendix A. Supplementary material

Supplementary data to this article can be found online at https://doi.org/10.1016/j.molliq.2023.123027.

References

[1] Z. Bargańska, J. Namieśnik, M. Ślebioda, Determination of antibiotic residues in honey, TrAC - Trends Anal. Chem. 30 (2011) 1035–1041, https://doi.org/10.1016/j.trac.2011.02.014.

[2] S. Tursynbolat, Y. Bakytkarim, J. Huang, L. Wang, Ultrasensitive electrochemical determination of metronidazole based on polydopamine/carboxylic multi-walled carbon nanotubes nanocomposites modified GCE, J. Pharm. Anal. 8 (2018) 124–130, https://doi.org/10.1016/j.jpha.2017.11.001.

[3] N. Di Tan, C. Lan, J.H. Yin, L. Meng, N. Xu, Selective detection of trace metronidazole by using a magnetic molecularly imprinted polymer-based fluorescent probe, Bull. Kor. Chem. Soc. 41 (2020) 60–65, https://doi.org/10.1002/bkcs.11918.

[4] G. Qin, D. Cao, X. Wan, X. Wang, Y. Kong, Polyvinylpyrrolidone-assisted synthesis of highly water-stable cadmium-based metal-organic framework nanosheets for the detection of metronidazole, RSC Adv. 11 (2021) 34842–34848, https://doi.org/10.1039/d1ra05349c.

[5] R. Moreno, S. Poyser, D. Meilak, A. Meo, S. Jenkins, V.K. Lazarov, G. Vallejo-Fernandez, S. Majetich, R.F.L. Evans, The role of faceting and elongation on the magnetic anisotropy of magnetite Fe3O4 nanocrystals, Sci. Rep. 10 (2020) 1–14, https://doi.org/10.1038/s41598-020-58976-7.

[6] Y. Liu, J. Liu, H. Tang, J. Liu, B. Xu, F. Yu, Y. Li, Fabrication of highly sensitive and selective electrochemical sensor by using optimized molecularly imprinted polymers on multi-walled carbon nanotubes for metronidazole measurement, Sens Actuat. B Chem. 206 (2015) 647–652, https://doi.org/10.1016/j.snb.2014.10.019.

[7] X. Yang, M. Liu, Y. Yin, F. Tang, H. Xu, X. Liao, Green, Hydrothermal Synthesis of Fluorescent Carbon Nanodots from Gardenia, Enabling the Detection of Metronidazole in Pharmaceuticals and Rabbit Plasma, Sensors. 18 (2018) 964. https://doi.org/10.3390/s18040964.

[8] L. Li, Z. Qiu, Y. Qi, D. Zhao, I. Ali, C. Sun, L. Xu, Z. Zheng, C. Ma, AuNPs/NiFe-LDHs-assisted laser desorption/ionization mass spectrometry for efficient analysis of metronidazole and its metabolites in water samples, J. Hazard. Mater. 423 (2022), 126893, https://doi.org/10.1016/j.jhazmat.2021.126893.

[9] K.K. Abdel Hady, R.A. Abdel Salam, G.M. Hadad, E.A. Abdel Hameed, Simultaneous HPLC determination of vildagliptin, ampicillin, sulbactam and metronidazole in pharmaceutical dosage forms and human urine, J. Iran. Chem. Soc. 18 (2021) 729–738, https://doi.org/10.1007/s13738-020-02065-z.

[10] S. Patze, U. Huebner, F. Liebold, K. Weber, D. Cialla-May, J. Popp, SERS as an analytical tool in environmental science: the detection of sulfamethoxazole in the nanomolar range by applying a microfluidic cartridge setup, Anal. Chim. Acta 949 (2017) 1–7, https://doi.org/10.1016/j.aca.2016.10.009.

[11] M.I. Gadallah, H.R.H. Ali, H.F. Askal, G.A. Saleh, Innovative HPTLC-densitometric method for therapeutic monitoring of meropenem and metronidazole in acute pancreatic patients, Microchem. J. 146 (2019) 940–947, https://doi.org/10.1016/j.microc.2019.02.011.

[12] J. Zhao, X. Pan, X. Sun, W. Pan, G. Yu, J. Wang, Detection of metronidazole in honey and metronidazole tablets using carbon dots-based sensor via the inner filter effect, Luminescence 33 (2018) 704–712, https://doi.org/10.1002/bio.3467.

[13] X. Yang, M. Liu, Y. Yin, F. Tang, H. Xu, X. Liao, Green, hydrothermal synthesis of fluorescent carbon nanodots from gardenia, enabling the detection of metronidazole in pharmaceuticals and rabbit plasma, Sensors (Switzerland). 18 (2018), https://doi.org/10.3390/s18040964.

[14] A. Lamaoui, A.A. Lahcen, J.J. García-Guzmán, J.M. Palacios-Santander, L. Cubillana-Aguilera, A. Amine, Study of solvent effect on the synthesis of magnetic molecularly imprinted polymers based on ultrasound probe: application for sulfonamide detection, Ultrason. Sonochem. 58 (2019), 104670, https://doi.org/10.1016/j.ultsonch.2019.104670.

[15] M. Wang, M. Gao, L. Deng, X. Kang, K. Zhang, Q. Fu, Z. Xia, D. Gao, A sensitive and selective fluorescent sensor for 2,4,6-trinitrophenol detection based on the composite material of magnetic covalent organic frameworks, molecularly imprinted polymers and carbon dots, Microchem. J. 154 (2020), 104590, https://doi.org/10.1016/j.microc.2019.104590.

[16] X. Zhang, S. Yang, W. Chen, Y. Li, Y. Wei, A. Luo, Magnetic fluorescence molecularly imprinted polymer based on FeOx/ZnS nanocomposites for highly selective sensing of bisphenol A, Polymers (Basel). 11 (2019), https://doi.org/10.3390/polym11071210.

[17] X. Lv, X. Xue, Y. Huang, Z. Zhuang, Z. Lin, The relationship between photoluminescence (PL) decay and crystal growth kinetics in thioglycolic acid (TGA) capped CdTe quantum dots (QDs), PCCP 16 (2014) 11747–11753, https://doi.org/10.1039/c4cp00765d.

[18] R.G. Machicote, M.A. Castillo, M.E. Pacheco, L. Bruzzone, A molecular imprinted polymer as a flow-Through optical sensor for oxazepam, J. Anal. Methods Chem. 2018 (2018), https://doi.org/10.1155/2018/6302609.

[19] L.N. Martínez Saavedra, Sínteses de polímeros molecularmente impressos para adsorção seletiva de quinolina em matriz orgânica, (2017) 129.

[20] C.A.M. Bonilla, M.H.T. Flórez, D.R. Molina Velasco, V.V. Kouznetsov, Surface characterization of thiol ligands on CdTe quantum dots: analysis by 1H NMR and DOSY, New J. Chem. 43 (2019) 8452–8458, https://doi.org/10.1039/c8nj05914d.

[21] E. Gharibshahi, Simulation, synthesis and optical properties of cadmium telluride (CdTe) semiconductor nanoparticles, Solid State Commun. 320 (2020), 114009, https://doi.org/10.1016/j.ssc.2020.114009.

[22] N.S. Moreno, Síntese de nanopartículas de magnetita dopadas com íons terras raras e avaliação das propriedades magneto-ópticas, (2020).

[23] S.K. Panda, I. Aggarwal, H. Kumar, L. Prasad, A. Kumar, A. Sharma, D.V.N. Vo, D. Van Thuan, V. Mishra, Magnetite nanoparticles as sorbents for dye removal: a review, Springer International Publishing (2021), https://doi.org/10.1007/s10311-020-01173-9.

[24] G. De Middeleer, P. Dubruel, S. De Saeger, Characterization of MIP and MIP functionalized surfaces: current state-of-the-art, TrAC Trends Anal. Chem. 76 (2016) 71–85, https://doi.org/10.1016/j.trac.2015.11.007.

[25] K. Zhang, Y. Wang, Q. Wen, Q. Huang, T. Li, Y. Zhang, D. Luo, Preparation and characterization of magnetic molecularly imprinted polymer for specific

adsorption of wheat gliadin, J. Mol. Struct. 1265 (2022), 133227, https://doi.org/10.1016/j.molstruc.2022.133227.
[26] A.M. Mostafa, S.J. Barton, S.P. Wren, J. Barker, Development of magnetic molecularly imprinted polymers for the extraction of salivary pepsin prior to analysis by a novel HPLC-SEC method, Polymer (Guildf). 261 (2022), 125417, https://doi.org/10.1016/j.polymer.2022.125417.
[27] Y. Cheng, H. Liu, J. Li, L. Kuang, G. Xu, Efficient and selective extraction of chlorogenic acid in juice samples using magnetic molecularly imprinted polymers, Microchem. J. (2022), 108110, https://doi.org/10.1016/j.microc.2022.108110.
[28] Y. Han, J. Tao, N. Ali, A. Khan, S. Malik, H. Khan, C. Yu, Y. Yang, M. Bilal, A. A. Mohamed, Molecularly imprinted polymers as the epitome of excellence in multiple fields, Eur. Polym. J. 179 (2022), 111582, https://doi.org/10.1016/j.eurpolymj.2022.111582.
[29] O. Çelik, Y. Saylan, I. Göktürk, F. Yılmaz, A. Denizli, A surface plasmon resonance sensor with synthetic receptors decorated on graphene oxide for selective detection of benzylpenicillin, Talanta 253 (2023), 123939, https://doi.org/10.1016/j.talanta.2022.123939.
[30] M.E. Çorman, C. Armutcu, T. Karasu, E. Özgür, L. Uzun, Highly selective benzo[a] pyrene detection even under competitive conditions with molecularly imprinted surface plasmon resonance sensor, Polycycl. Aromat. Compd. (2022) 1–14, https://doi.org/10.1080/10406638.2022.2080725.
[31] D. Balciunas, D. Plausinaitis, V. Ratautaite, A. Ramanaviciene, A. Ramanavicius, Towards electrochemical surface plasmon resonance sensor based on the molecularly imprinted polypyrrole for glyphosate sensing, Talanta 241 (2022), 123252, https://doi.org/10.1016/j.talanta.2022.123252.
[32] S. Basak, R. Venkatram, R.S. Singhal, Recent advances in the application of molecularly imprinted polymers (MIPs) in food analysis, Food Control 139 (2022), 109074, https://doi.org/10.1016/j.foodcont.2022.109074.
[33] W. Yang, Y. Ma, H. Sun, C. Huang, X. Shen, Molecularly imprinted polymers based optical fiber sensors: a review, TrAC Trends Anal. Chem. 152 (2022), 116608, https://doi.org/10.1016/j.trac.2022.116608.
[34] N. Cennamo, A.M. Bossi, F. Arcadio, D. Maniglio, L. Zeni, On the effect of soft molecularly imprinted nanoparticles receptors combined to nanoplasmonic probes for biomedical applications, Front. Bioeng. Biotechnol. 9 (2021), https://doi.org/10.3389/fbioe.2021.801489.
[35] N. Bereli, D. Çimen, S. Hüseynli, A. Denizli, Detection of amoxicillin residues in egg extract with a molecularly imprinted polymer on gold microchip using surface plasmon resonance and quartz crystal microbalance methods, J. Food Sci. 85 (2020) 4152–4160, https://doi.org/10.1111/1750-3841.15529.
[36] Ö. Kurç, D. Türkmen, Molecularly Imprinted polymers based surface plasmon resonance sensor for sulfamethoxazole detection, Photonic Sensors. 12 (2022), 220417, https://doi.org/10.1007/s13320-022-0658-5.
[37] Q. Zhang, L. Jing, J. Zhang, Y. Ren, Y. Wang, Y. Wang, T. Wei, B. Liedberg, Surface plasmon resonance sensor for femtomolar detection of testosterone with water-compatible macroporous molecularly imprinted film, Anal. Biochem. 463 (2014) 7–14, https://doi.org/10.1016/j.ab.2014.06.014.
[38] S.-W. Choi, H.-J. Chang, N. Lee, J.-H. Kim, H.S. Chun, Detection of Mycoestrogen zearalenone by a molecularly imprinted polypyrrole-based surface Plasmon resonance (SPR) sensor, J. Agric. Food Chem. 57 (2009) 1113–1118, https://doi.org/10.1021/jf804022p.
[39] J. Homola, Surface Plasmon resonance sensors for detection of chemical and biological species, Chem. Rev. 108 (2008) 462–493, https://doi.org/10.1021/cr068107d.
[40] J.C. Martinez, J. Murciano-calles, E.S. Cobos, M. Iglesias-bexiga, I. Luque, J. Ruiz-sanz, Isothermal Titration Calorimetry : Thermodynamic Analysis of the Binding Thermograms of Molecular Recognition Events by Using Equilibrium Models, in: Applications of Calorimetry in a Wide Context – Differential Scanning Calorimetry, Isothermal Titration Calorimetry and Microcalorimetry, 2013: pp. 73–104. https://doi.org/https://doi.org/10.5772/53311.
[41] L.T.A. da Rosa, I.F.S. Aversa, E. Raphael, A.S. Polo, A. Duarte, M.A. Schiavon, L. S. Virtuoso, Improving photoluminescence quantum yield of CdTe quantum dots using a binary solvent (Water + Glycerin) in the one-pot approach synthesis, J. Braz. Chem. Soc. 32 (2021) 860–868. https://doi.org/10.21577/0103-5053.20200237.
[42] M.G. Santos, D.T. de Carvalho, L.B. Caminitti, B.B.A. de Lima, M.H. da S. Cavalcanti, D.F.R. dos Santos, L.S. Virtuoso, D.B. Hirata, E.C. Figueiredo, Use of magnetic Fe3O4 nanoparticles coated with bovine serum albumin for the separation of lysozyme from chicken egg white, Food Chem. 353 (2021). https://doi.org/10.1016/j.foodchem.2021.129442.
[43] W. Stober, A. Fink, D. Ernst Bohn, Controlled Growth of Monodisperse Silica Spheres in the Micron Size Range 1, 1968.
[44] R. Long, T. Li, C. Tong, L. Wu, S. Shi, Molecularly imprinted polymers coated CdTe quantum dots with controllable particle size for fluorescent determination of p-coumaric acid, Talanta 196 (2019) 579–584, https://doi.org/10.1016/j.talanta.2019.01.007.
[45] R.B.M. Schasfoort, Handbook of Surface Plasmon Resonance, 2nd ed., 2017. https://doi.org/10.1039/9781788010283.
[46] C. das D. Aguiar, Y.L. Coelho, H.M.C. de Paula, L.N. Santa Rosa, L.S. Virtuoso, T.A. de O. Mendes, A.C. dos S. Pires, L.H.M. da Silva, Thermodynamic and kinetic insights into the interactions between functionalized CdTe quantum dots and human serum albumin: A surface plasmon resonance approach, Int J Biol Macromol. 184 (2021) 990–999. https://doi.org/10.1016/j.ijbiomac.2021.06.158.
[47] H. Eyring, The activated complex and the absolute rate of chemical reactions, Chem. Rev. 17 (1935) 65–77, https://doi.org/10.1021/cr60056a006.
[48] G. Lente, I. Fábián, A.J. Poë, A common misconception about the Eyring equation, New J. Chem. 29 (2005) 759–760, https://doi.org/10.1039/b501687h.
[49] S. Glöckner, G. Klebe, Simultaneous determination of thermodynamic and kinetic data by isothermal titration calorimetry, Biochim. Biophys. Acta Gen. Subj. 2021 (1865) 1–7, https://doi.org/10.1016/j.bbagen.2020.129772.
[50] L. Baranauskiene, T.C. Kuo, W.Y. Chen, D. Matulis, Isothermal titration calorimetry for characterization of recombinant proteins, Curr. Opin. Biotechnol. 55 (2019) 9–15, https://doi.org/10.1016/j.copbio.2018.06.003.
[51] J.K. Awino, Y. Zhao, Molecularly imprinted nanoparticles as tailor-made sensors for small fluorescent molecules, Chem. Commun. 50 (2014) 5752–5755, https://doi.org/10.1039/c4cc01516a.
[52] A. Nagy-Szakolczai, Z. Dorkó, B. Tóth, G. Horvai, New methods to study the behavior of molecularly imprinted polymers in aprotic solvents, Polymers (Basel). 10 (2018) 1–12, https://doi.org/10.3390/polym10091015.
[53] W.P. Fish, J. Ferreira, R.D. Sheardy, N.H. Snow, T.P. O'Brien, Rational design of an imprinted polymer: Maximizing selectivity by optimizing the monomer-template ratio for a cinchonidine MIP, prior to polymerization, using microcalorimetry, J. Liq. Chromatogr. Relat. Technol. 28 (2005) 1–15, https://doi.org/10.1081/JLC-200038551.
[54] M. Kudrat-E-Zahan, Z. Yıldız, S. Çolak, E. Yıldırım, Ö. Toplan, TGA-capped CdTe quantum dots: synthesis, characterization and stabilization in polymer matrix by using a water dispersible polymer, 2018.
[55] A.M. Santos, A. Wong, T.M. Prado, E.L. Fava, O. Fatibello-Filho, M.D.P. T. Sotomayor, F.C. Moraes, Voltammetric determination of ethinylestradiol using screen-printed electrode modified with functionalized graphene, graphene quantum dots and magnetic nanoparticles coated with molecularly imprinted polymers, Talanta 224 (2021), 121804, https://doi.org/10.1016/j.talanta.2020.121804.
[56] W. Xu, Y. Wang, W. Huang, L. Yu, Y. Yang, H. Liu, W. Yang, Computer-aided design and synthesis of CdTe@SiO2 core–shell molecularly imprinted polymers as a fluorescent sensor for the selective determination of sulfamethoxazole in milk and lake water, J. Sep. Sci. 40 (2017) 1091–1098, https://doi.org/10.1002/jssc.201601180.
[57] N. Tarannum, S. Khatoon, B.B. Dzantiev, Perspective and application of molecular imprinting approach for antibiotic detection in food and environmental samples: a critical review, Food Control 118 (2020) 1–19, https://doi.org/10.1016/j.foodcont.2020.107381.
[58] J.J. Belbruno, Molecularly imprinted polymers, Chem. Rev. 119 (2019) 94–119, https://doi.org/10.1021/acs.chemrev.8b00171.
[59] J. de P. Rezende, E.A. Hudson, H.M.C. de Paula, R.S. Meinel, A.D. da Silva, A.C. dos S. Pires, L.H.M. da Silva, Human serum albumin-resveratrol complex formation: Effect of the phenolic chemical structure on the kinetic and thermodynamic parameters of the interactions, Food Chem. 307 (2020) 125514. https://doi.org/10.1016/j.foodchem.2019.125514.
[60] K.F. Pratama, M.E.R. Manik, D. Rahayu, A.N. Hasanah, Effect of the molecularly imprinted polymer component ratio on analytical performance, Chem Pharm Bull (Tokyo). 68 (2020) 1013–1024, https://doi.org/10.1248/cpb.c20-00551.
[61] A. Fernández-Ramos, J.A. Miller, S.J. Klippenstein, D.G. Truhlar, Modeling the kinetics of bimolecular reactions, Chem. Rev. 106 (2006) 4518–4584, https://doi.org/10.1021/cr050205w.
[62] S. Gul, G.W. Mellor, E.W. Thomas, K. Brocklehurst, Temperature-dependences of the kinetics of reactions of papain and actinidin with a series of reactivity probes differing in key molecular recognition features, Biochem. J 396 (2006) 17–21, https://doi.org/10.1042/BJ20051501.
[63] Z. Cui, Z. Li, Y. Jin, T. Ren, J. Chen, X. Wang, K. Zhong, L. Tang, Y. Tang, M. Cao, Novel magnetic fluorescence probe based on carbon quantum dots-doped molecularly imprinted polymer for AHLs signaling molecules sensing in fish juice and milk, Food Chem. 328 (2020), 127063, https://doi.org/10.1016/j.foodchem.2020.127063.